Materials Science & Engineering A 637 (2015) 189–200

Contents lists available at ScienceDirect

Materials Science & Engineering A

journal homepage: www.elsevier.com/locate/msea

Interaction between recrystallization and strain-induced precipitation in a high Nb- and N-bearing austenitic stainless steel: Influence of the interpass time

M.B.R. Silva [a,*], J. Gallego [b], J.M. Cabrera [c,d], O. Balancin [a], A.M. Jorge Jr [a,*]

[a] Department of Materials Engineering, UFSCar, Via Washington Luis, Km 235, 13565-905 São Carlos, SP, Brazil
[b] Department of Mechanical Engineering, UNESP, Avenida Brasil, 56, 15385-000 Ilha Solteira, SP, Brazil
[c] Department of Materials Science and Metallurgical Engineering, Polytechnic University of Catalunya, Avenida Diagonal 647, 08028 Barcelona, Spain
[d] Fundacio CTM Centre Tecnologic, Plaza de la Ciencia 2, 08243 Manresa, Spain

ARTICLE INFO

Article history:
Received 10 December 2014
Received in revised form
14 April 2015
Accepted 19 April 2015
Available online 28 April 2015

Keywords:
Hot mechanical behavior
Recrystallization
Grain refinement
Niobium
Precipitation
Stainless steel

ABSTRACT

In this work, we studied the influence of the interpass time (20 and 5 s) on the interaction between recrystallization and strain-induced precipitation occurring during multiple passes' deformations under continuous cooling conditions in a high niobium- and nitrogen-bearing austenitic stainless steel (ISO 5832-9). The correlation between microstructure evolution and hot mechanical properties was performed by physical simulation using hot torsion tests. The microstructure evolution was analyzed by optical microscopy, transmission electron microscopy and electron back scattered diffraction (EBSD). This technique indicated that dynamic recrystallization occurred at the first passes promoting an excellent grain refinement. On the other hand, shorter interpass time (5 s) allowed higher volume fraction of smallest precipitates than larger interpass time (20 s). After soaking, only TiNbN precipitates were found, whereas, Z-phase (CrNbN) and NbN were formed during thermomechanical processing. Particles with sizes between 20 and 50 nm were effective to pin grain boundaries and dislocations.

1. Introduction

Austenitic stainless steels are widely used due to a favorable combination of properties such as: strength, corrosion resistance, workability and weldability. They have many industrial applications and represent a significant volume of the world production of metallic alloys. Among these steels are those with high content of nitrogen, which improves mechanical properties due to solid solution hardening [1,2]. Some advantages of high-nitrogen steels are: elevated yield stress; excellent combination of high resistance to the fracture and toughness; resistance to the formation of strain-induced martensite; low magnetic permeability, avoiding the formation of ferromagnetic phases; and good corrosion properties, improving pitting corrosion resistance [3]. The nitrogen is a strong austenite stabilizer, enabling reducing the amount of Ni for the austenite stabilization and, additionally, retarding the precipitation of chromium- and molybdenum-rich phases (σ, χ, $M_{23}C_6$ phases), which are known for spoiling certain properties, mainly due to consumption of chromium from the matrix, causing the increase of sensitization [4,5].

An important application of this kind of steel is as orthopedic implants due to its good strength and corrosion resistance and especially due to its relatively low cost. To date, the most widely used steel in the implants field is the ASTM F138, but its susceptibility to localized corrosion limits its use in permanent orthopedic implants [6]. The ISO 5832-9 alloy, an austenitic stainless steel with high nitrogen and niobium, has been used as an alternative to ASTM F138 in more severe conditions.

Independent of the employed processing, grain refinement and strain accumulation are the keys for achievement of good properties of the rolled and forged materials [7]. It is well known that the reduction of grain size will introduce homogeneity in the deformation [8,9] and, in addition, the grain refinement increases the strength of an alloy, according to the Hall–Petch's relationship, leading to a better mechanical behavior after processing. In fact, reduction of grain size is the unique mechanism that increases both strength and toughness [10,11]. In turn, strain accumulation is related to the generation and annihilation of dislocations, which is facilitated by the presence of precipitates.

In order to obtain finer grains after thermomechanical treatments, it is necessary to study the processing history, whose conditions will control the final size of the recrystallized grain. As it is

* Corresponding authors.
E-mail addresses: marianabdrs@gmail.com (M.B.R. Silva), moreira@dema.ufscar.br (A.M. Jorge Jr).

http://dx.doi.org/10.1016/j.msea.2015.04.049
0921-5093/

well known, one of the approaches for obtaining fine grains is through fine precipitation occurring during the recrystallization process [12–14]. This will hinder the mobility of boundaries recently formed by dynamic recrystallization and even during time intervals between deformation passes, where static and metadynamic recrystallization can take place. In general, plastic deformation generates high-energy preferential sites for precipitation [9,12], such as dislocations, dislocation forests, cells and subgrains and even lately dynamic recrystallized grain boundaries or, in other words, the interaction between precipitation and recrystallization can control the refinement process. Hence, depending on the strain rate and temperature, different amounts of precipitates will be formed and distinct hot mechanical properties will be acquired during deformation, producing diverse flow-stress behaviors. Furthermore, depending on the interpass time, the precipitates can either grow or miss their coherence. Thus, distinct flow-stress behaviors will be found depending on different interpass times.

The scientific features needed to control the microstructure evolution during thermomechanical processing of ISO 5832-9 steel, which has some similarities with microalloyed steels, are not well known [15], mainly the interaction between precipitation and recrystallization in this steel has received scarce attention. Particularly, there is evidence that precipitation of second phase particles (mostly Z-phase (CrNbN)) takes place during hot working [15,16]. The amount, size, distribution and morphology of these particles have marked influence on the materials' properties [9]. The presence of fine precipitates with small spacing between them tends to pin grain boundaries and to inhibit static and dynamic recrystallization, while the coarsening of these particles may deteriorate some properties such as fatigue and corrosion resistance [17,18]. In order to optimize strength and corrosion resistances, an appropriate microstructure must be attained, which in turn depends on the chemical composition and previous thermomechanical processing history.

Therefore, as each pass is dependent on the previous one and also of the interpass time, the dynamic answer of the material must be accessed. This will provide a more precise behavior on the flow-stress, which will lead to a more precise analysis on the whole dynamic mechanical behavior.

Based on the limitations of the available information, present study was conducted to investigate the influence of interpass time on the interaction between recrystallization and precipitation in an austenitic stainless steel with high content of Nb and N. To access dynamic information on the mechanical behavior of the previous pass, the influence of the time, and their influence on the subsequent passes, hot torsion tests were used.

2. Material

The material analyzed in this investigation was a high-niobium and high-nitrogen austenitic stainless steel, type ISO 5832-9, whose chemical composition is presented in Table 1. The alloy was supplied by Villares Metals (Brazil) in the form of hot rolled bars with a diameter of 20 mm, annealed at 1030 °C for 60 min and water cooled. Cylindrical specimens with 5 mm of effective radius and 10 mm length in the reduced central gauge section were machined out from the bars. The mechanical tests were performed on a computerized hot torsion machine. The samples were heated in an induction heating furnace, directly coupled to the machine. The data were processed using a software that imposes and controls parameters as temperature, holding time, amount of deformation, strain rate and interpass times. The temperature was measured using an optical pyrometer.

The samples were hot strained by torsion testing with multiple passes under continuous cooling conditions. The specimens were heated to 1250 °C at a rate of 5.5 °C/s and hold at this temperature for 300 s. Then, they were subjected to successive passes with true strain (ε) of 0.3, strain rate of 1.0 s^{-1} and interpass times of 5 s or 20 s. The cooling rates were 240 °C/min (for interpass time of 5 s) and 60 °C/min (for interpass time of 20 s); in a determined pass, the samples were at the same temperature independent of the interpass times. These tests were interrupted after the 2, 10 and 13 passes, and the samples were water quenched.

The samples were characterized by optical microscopy, electron backscatter diffraction (EBSD) and transmission electron microscopy (TEM). The microstructure was observed in a longitudinal plane, below the deformed surface. TEM analyses were performed in an FEI Tecnai G2-F20 (200 kV), equipped with an EDX detector (EDAX).

The microstructures were revealed by electrochemical etching using a solution of nitric acid (65%), density current of 0.5 A/cm^2 and times ranging from 20 to 60 s, depending on the microstructure. Quantitative metallography was performed by measuring the Feret diameter (diameter of a circle having same area of the object) with a count of at least 400 grains, using the image analyzer software AnalysisFive. The average grain size also includes twins as grain boundaries.

Carbon replicas were prepared by etching the matrix following the same procedures as for optical microscopy. After that, a thin carbon layer was evaporated on the etched surface and then the carbon layer containing precipitates was extracted from the surface by electrolytic etching and supported on a 300-mesh Cu grid. In each replica, a population of no less 200 particles was counted, and their size was measured with the aim of calculating the mean size, particle density and volume fraction. The volume fraction was calculated by the Maniar's method [19]. Thin foils samples were also prepared by electrolytic polishing using a solution of acetic acid (95%) and perchloric acid (5%), at room temperature (~25 °C).

Electron diffraction analyses were performed for each precipitate using at least, two different axes and the indexations were done by calculation from measurements between points and angles, as usual, and confirmed with the help of JEMS software [20].

For EBSD observations, the specimens were electropolished in a solution of 5% of perchloric acid in acetic acid at room temperature (~25 °C) using a 35 V DC and time of ~20 s. The EBSD scans were performed in an INSPECT S50 (FEI COMPANY™) SEM microscope equipped with an EBSD system (EDAX-AMETEK™).

Additionally, microhardness tests were performed on larger particles+matrix and on smaller particles+matrix after a soaking time and after two and six passes of deformation. This was done to verify the influence of such kinds of particles on the related stress fields. The microhardness tests were performed in the Future-Tech FM-800 hardness equipment with a Vickers indenter by using a load of 25 g.

Table 1
Chemical composition of austenitic stainless steel (wt%).

C	Si	Mn	Ni	Cr	Mo	S	P	Cu	N	Nb	V	Ti	Fe
0.031	0.38	3.98	10.43	20.43	2.46	0.0018	0.022	0.12	0.35	0.28	0.12	0.005	Bal.

3. Results

3.1. Mechanical behavior

Fig. 1 displays flow stress curves obtained for the ISO 5832-9 steel deformed with interpass times of 20 and 5 s. As a general trend, the flow stress increases with the pass number, especially after the third pass. In the first approach, the increases of the stress level may be associated with the temperature decreasing during the processing. This dependence is more evidently illustrated using the mean flow stress (MFS) vs. the inverse of the absolute temperature plots [21], as displayed in Fig. 2. This figure clearly shows that the stress level depends on the deformation temperature, and that the slope of MFS vs. $1/T$ takes three different values as the deformation temperature decreases below a transition temperature at about 1100 °C, creating three distinct regions. At high temperatures (regions I and II), the material can be completely recrystallized during deformations and interpass times and there is no strain accumulation from pass to pass. At the highest temperatures (first 2 passes, region I), the material undergoes a strain hardening in the first pass and then is severely softened by dynamic recrystallization (DRX) in the first and in the subsequent passes. This specific behavior will be discussed later. After the third pass, apparently there is a stabilization of the microstructure and the stresses start to increase again due to the temperature effect. However, at lower temperatures (region III) the increase in the slope of the MFS vs. $1/T$ is an indication that there is one additional strengthening mechanism.

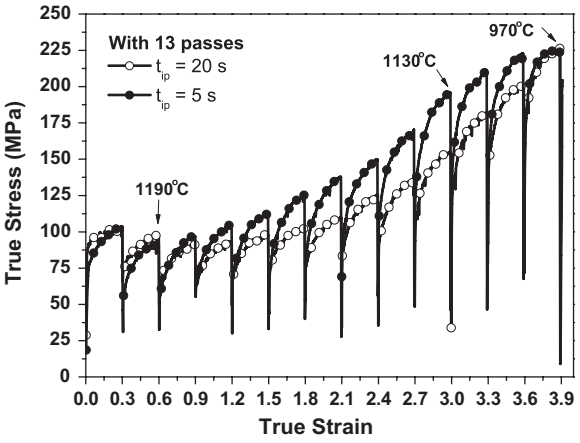

Fig. 1. Flow stress curves for the stainless steel with 13 passes and interpass times of 20 and 5 s, indicating the temperatures where tests were interrupted (1190 °C – 2nd pass, 1130 °C – 10th pass and 970 °C – 13th pass). (t_{ip}=interpass time).

3.2. Microstructural evolution

Fig. 3 depicts microstructures observed by optical microscopy in different conditions. Fig. 3a shows the as-received condition, showing a grain size with a mean value of 14.4 μm. The microstructure observed after the soaking time, which was considered as the starting microstructure, is shown in Fig. 3b and consists of coarse grains with an average grain diameter (d) of 61.8 μm and many annealing twins. Furthermore, grain size heterogeneity is observed as well a large number of coarse particles with different sizes, particularly inside the grains. These particles were not dissolved during the reheating. Since all samples were reheated at the same temperature and during the same holding time before testing, they all presented the same initial microstructure.

After the second pass with interpass time of 20 s, the material was recovered and recrystallized showing an average grain size of about 30 μm (Fig. 3c), and, therefore, some grain refinement was achieved. However, the refinement observed with interpass time of 5 s (Fig. 3d) was greater than that with 20 s. Below the transition temperature (~1100 °C), inside the region III in Fig. 2b, an intense grain refinement was observed as illustrated in Fig. 3e–g. It is worth noting that the microstructures consisted of smaller (recrystallized) grains, and some non-recrystallized but elongated (pancake) grains, indicating that full recrystallization was not achieved. The average grain size after the 10th pass and interpass time of 20 s was 11.8 μm (Fig. 3e) and at the end of the 13th pass was 9.5 μm (Fig. 3f); smaller grain size was observed (5.1 μm) as the interpass time was reduced to 5 s (Fig. 3g).

Statistical distributions of grain sizes were based on data from at least 400 grains and the fitted curves for the grain size distribution for all conditions are displayed in Fig. 4. It is worth noting again that grain refinement was noticed at increasing pass numbers and at decreasing interpass time. The broad initial grain size distribution became narrower as deformation was applied.

EBSD analyses were performed to improve the microstructure observation, mainly in conditions that exhibited more intense grain refinement and as an indirect way of measuring the recrystallized fraction (taken into account the fraction of high-angle grain boundaries). Fig. 5 shows images for 10th pass after interpass time of

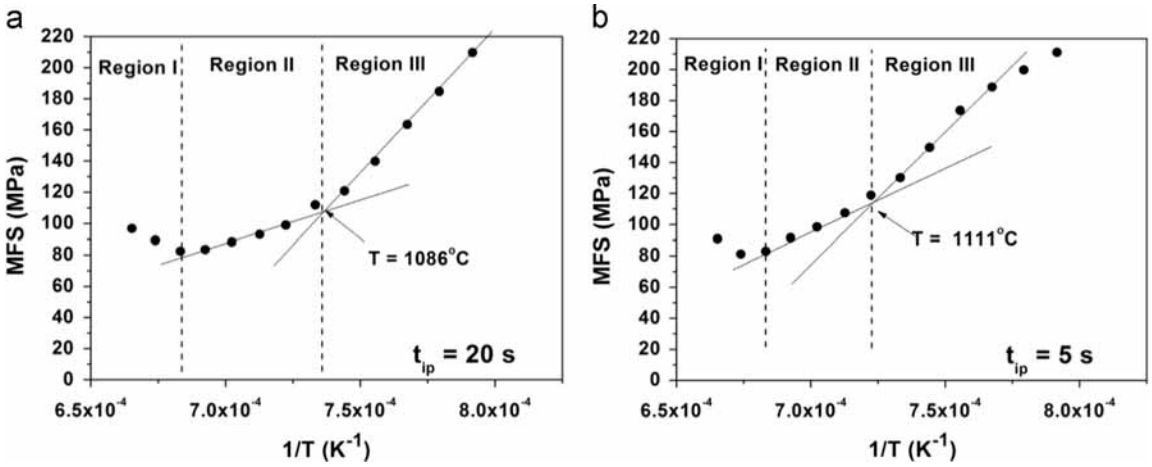

Fig. 2. Dependence of the mean flow stress (MFS) with the inverse of the absolute temperature. (a) interpass time of 20 s. (b) interpass time of 5 s.

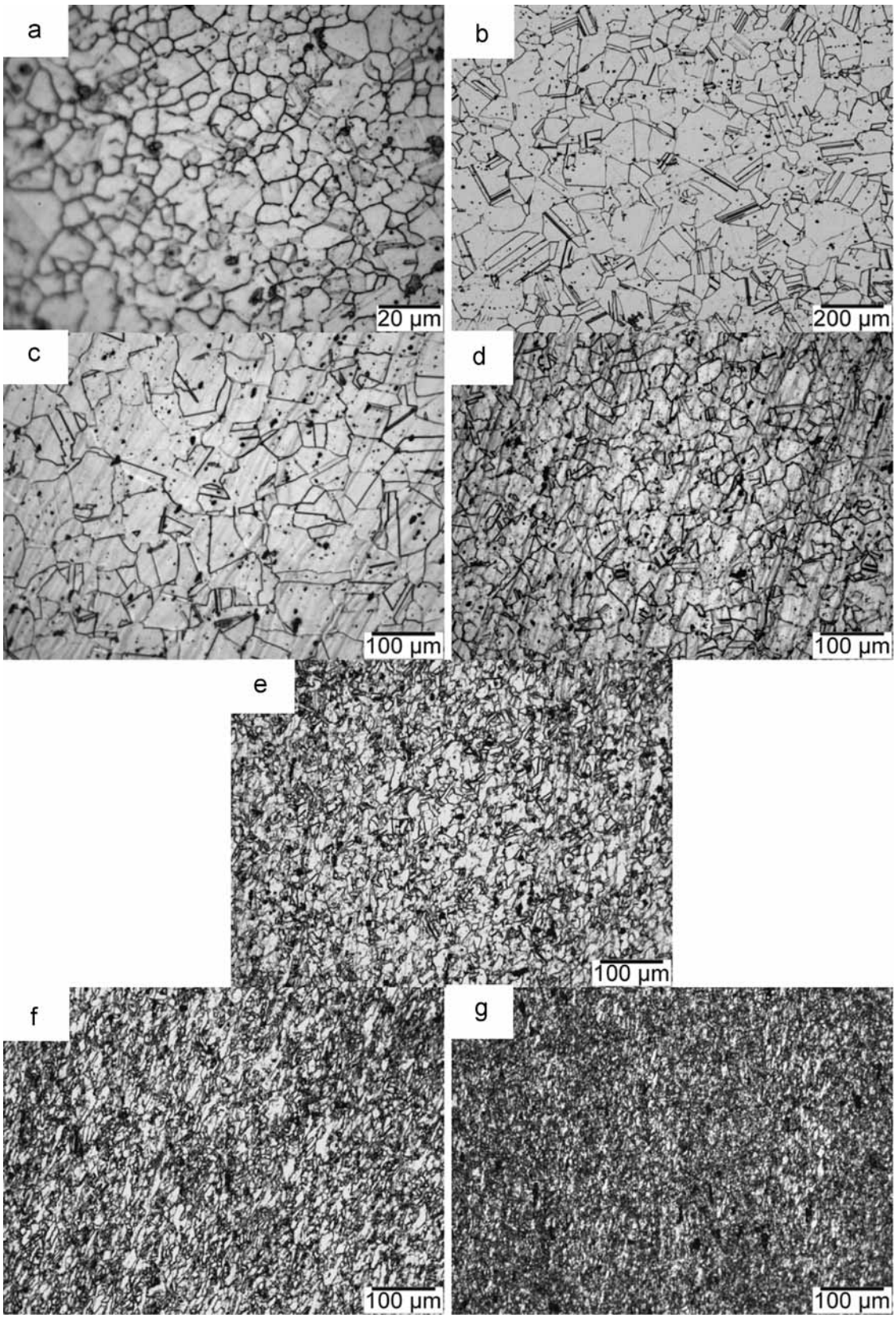

Fig. 3. Optical micrographs: (a) as-received condition. (b) $T_{soak}=1250$ °C (5 min). (c) After the second pass and $t_{ip}=20$ s. (d) After the second pass with $t_{ip}=5$ s. (e) After the 10th pass and $t_{ip}=20$ s. (f) After the 13th pass and $t_{ip}=20$ s. (g) After the 13th pass and $t_{ip}=5$ s.

20 s. The map of the Inverse Pole Figure (IPF) is shown in Fig. 5a, and the colors are indexed in the IPF shown in the inset of the figure. It can be observed that there is no preferential orientation after processing; the same fact was observed for all analyzed conditions. Fig. 5b shows the grain size distribution, which confirms the sizes observed by optical microscopy.

The image quality (IQ) map is shown in Fig. 5c. In this micrograph, the gray scale at each point in the image reflects the good quality of the corresponding Electron BackScattered Pattern (EBSP), which is related to the sample preparation and quality of indexation. Dark points are associated with poor patterns (in this case, mainly second phase particles) due to the absence of indexation, while light points are associated with excellent patterns. Grain and twin boundaries, precipitates within and at grain boundaries and larger non-dissolved second phase particles are also visible in this picture. Grain boundaries with misorientations greater than 15° are overlaid on the gray scale image, where grains of different sizes are observed (most of them are smaller than 15 μm) and some grains have pancake shape (deformed). An Orientation Image Mapping (OIM) analysis is shown in Fig. 5d, where the fraction of high ($\theta > 15°$-blue lines) and low ($2° < \theta < 15°$°-red lines) angles grain boundaries are presented. After the 10th pass and holding time of 20 s, the fraction of high angle was smaller than 60% indicating partial recrystallization.

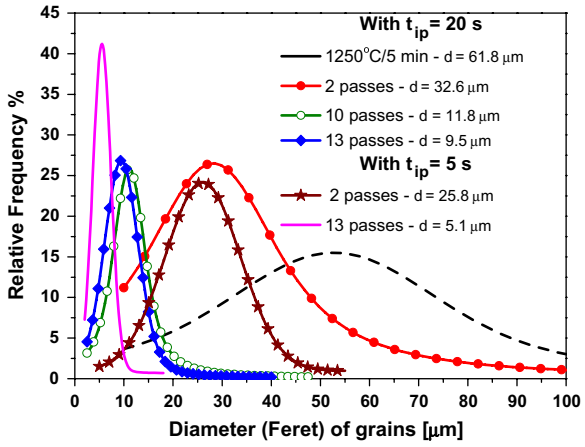

Fig. 4. Statistical distribution of grain sizes.

In order to verify the occurrence of dynamic recrystallization, a complementary experiment was conducted, in which one sample with 2 passes and 20 s of interpass time was quenched immediately after the second deformation step. Fig. 6a shows the IQ map and Fig. 6b the OIM analysis. The microstructure consists of elongated grains, and some of these are surrounded by small grains in a growing process, characterizing the necklace mechanism, which is typical of dynamic recrystallization [22,23] indicating that, under the

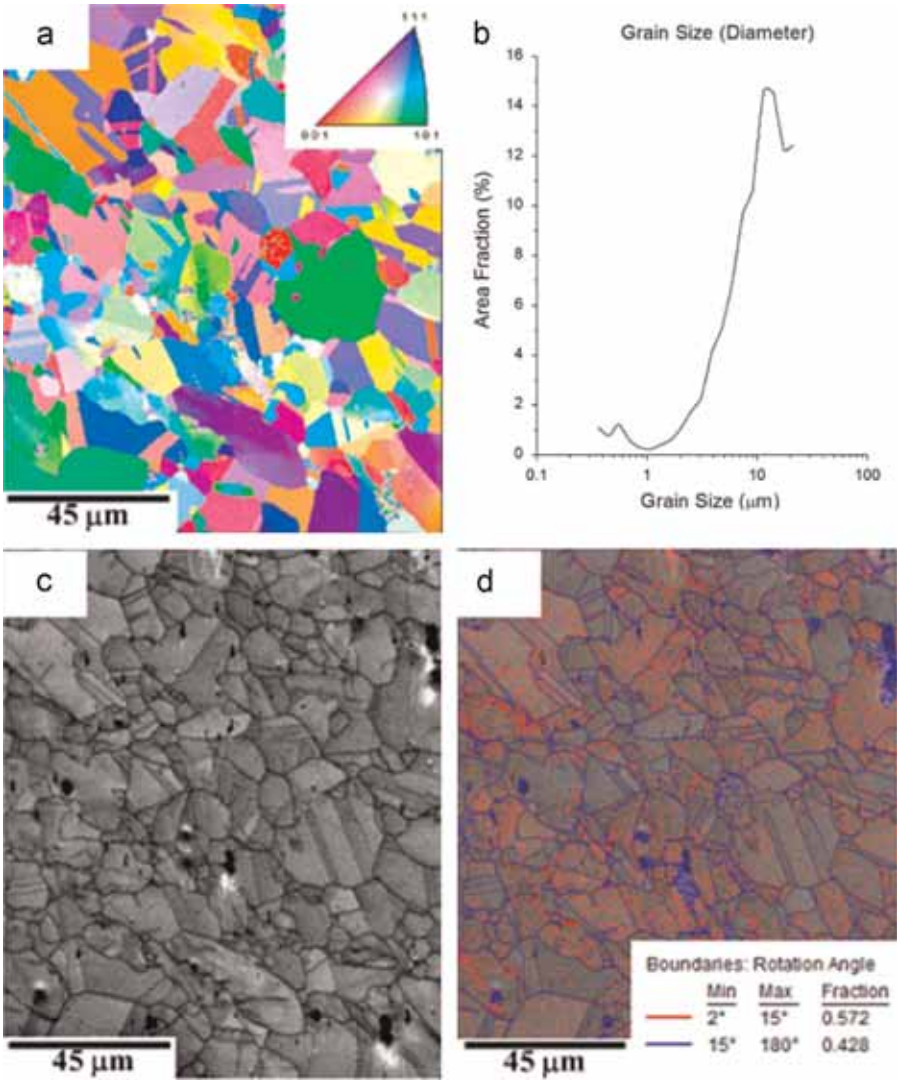

Fig. 5. Images and graph obtained from the EBSD analysis after 10 passes and interpass time of 20 s. (a) Map of the inverse pole figure (IPF) (color orientation indexation is shown in the IPF presented in the inset). (b) Grain size distribution. (c) Image quality map. (d) Orientation Image Mapping (OIM) showing high angle (grains-$\theta > 15°$-blue lines) and low angle (subgrains-$2 < \theta < 15°$-red lines) grain boundaries. (For interpretation of the references to color in this figure legend, the reader is referred to the web version of this article).

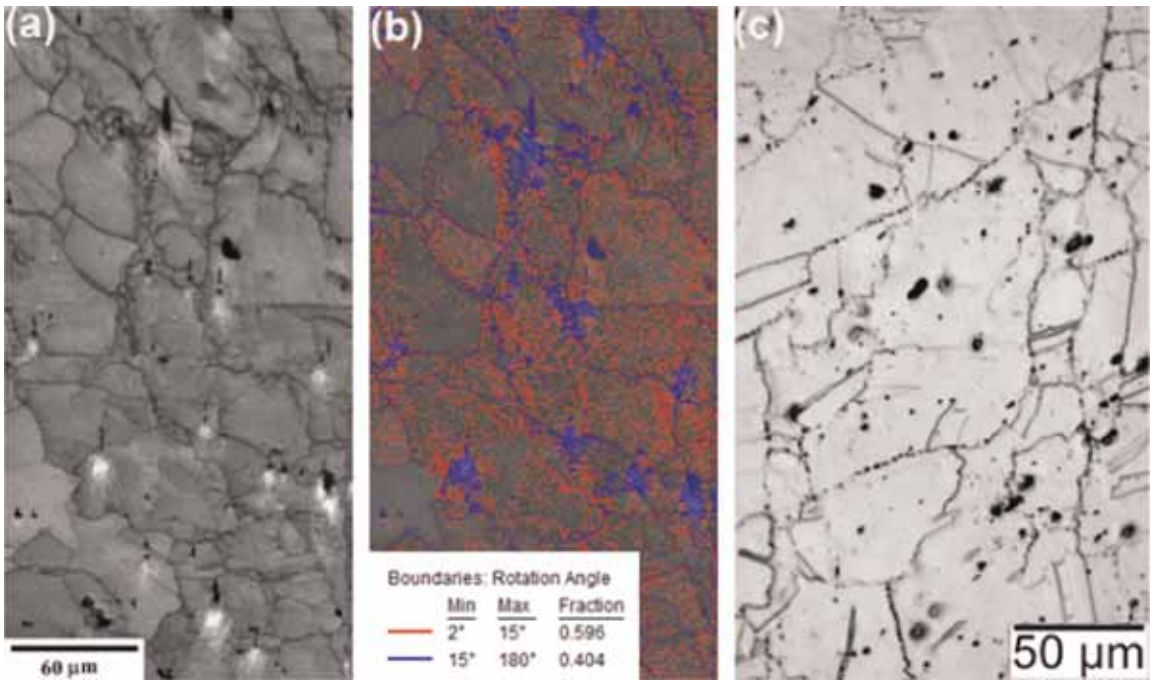

Fig. 6. Images obtained from the EBSD analysis from one sample with 2 passes and 20 s of interpass time quenched immediately after the second deformation. (a) Image quality map. (b) OIM showing high angle ($\theta > 15°$-blue lines) and low angle ($2 < \theta < 15°$-red lines) grain boundaries. (c) Optical micrograph. (For interpretation of the references to color in this figure legend, the reader is referred to the web version of this article.)

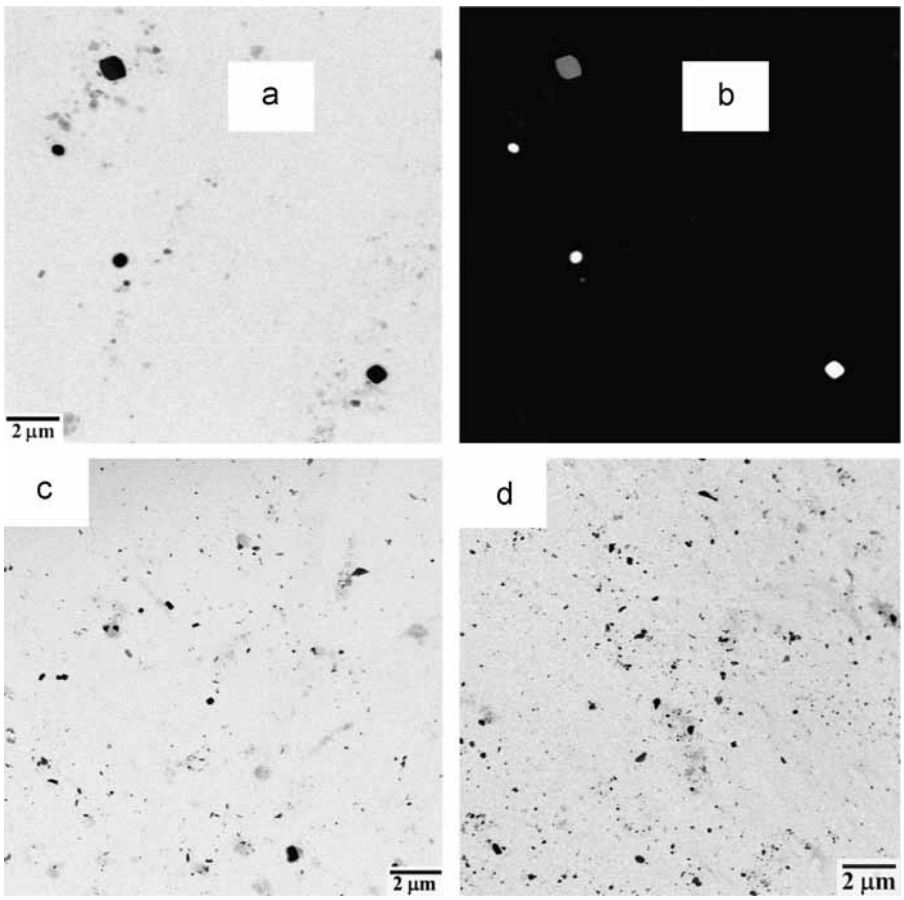

Fig. 7. Scanning Transmission Electron Microscopy (STEM) micrographs from carbon replica: (a) Bright Field STEM image for T_{soak} = 1250 °C (5 min). (b) HAADF image of the region analyzed in Fig. 7a. (c) On cooling with t_{ip} = 20 s after the 10th pass. (d) On cooling with t_{ip} = 20 s after the 13th pass.

analyzed condition, dynamic recrystallization took place. The data displayed in Fig. 6b shows that the amount of high-angle grain boundaries is around 60%.

Fig. 6c illustrates one optical micrograph of the above condition. It is worth noting that many particles were placed at grain boundaries, which was probably the result of breakage and redistribution of non-dissolved large particles (within the grains) after deformation. However, they had very large sizes and it is here assumed that they were not effective in controlling recrystallization or grain growth. These coarse particles, resulted of incomplete dissolution during the soaking time, would be acting as particle reinforcement of the matrix, mainly in the first two passes, before their total breakage and redistribution. As previously mentioned, the behavior of the two initial passes will be further discussed later.

3.3. Precipitation evolution

The precipitation behavior observed after extraction by carbon replica is shown in Fig. 7. Fig. 7a shows Bright Field (BF) Scanning Transmission Microscopy (STEM) image depicting a region of the sample after soaking, where few large precipitates can be seen. In this condition, the extracted precipitates are either spherical or squares with rounded corners. However, as it will be shown later in the thin foil analysis, large elongated particles were not extracted by the carbon replica technique. Statistically, they were not considered even because they will not influence in the grain growth control. This can be promptly observed by the grain size evolution (Fig. 3), where grains have grown from 14.4 μm to 61.8 μm in the presence of large particles (after soaking), or where grains were highly refined only after copious and extremely fine precipitation within region 3.

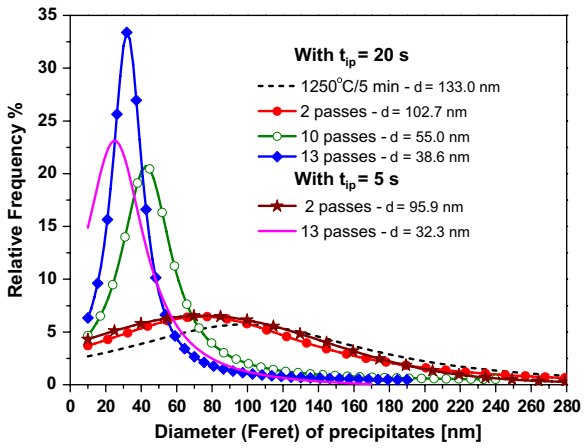

Fig. 8. Graph of statistical distribution of precipitate size comparing all the analyzed conditions.

Fig. 7b shows the high-angle annular dark-field (HAADF) STEM image of the same region of Fig. 7a. An HAADF detector will present gray tones proportional to the atomic number or to the phase density, also known as Z-contrast, producing images with excellent contrast. This figure illustrates how the images were analyzed, i.e., how the precipitates were distinguished from thicker carbon particles produced during the carbon deposition process in the replica extraction method.

Fig. 7c and d shows BF-STEM illustrating regions of intense precipitation observed after the transition temperatures, as defined in Fig. 2. Both images were obtained from samples strained with interpass time of 20 s, with Fig. 7c attained 20 s after the 10th pass and Fig. 7d attained 20 s after the 13th pass. Different shapes (spherical, squared and elongated) and sizes were noticed for all conditions. Fig. 8 summarizes the precipitate size distribution for all analyzed conditions. As observed for grain sizes, the precipitates size decreases with the progress of deformation, and smaller particles were obtained with the shortest interpass time.

Some precipitates with different shapes and sizes, extracted by carbon replicas, were analyzed by electron diffraction and energy dispersive X-ray, and the results are shown in Figs. 9 and 10. Precipitates with different morphologies at the end of soaking time are illustrated in Fig. 9a; an EDX spectrum is shown in Fig. 9b, and one selected area electron diffraction pattern (SAEDP) is shown in Fig. 9c. From the EDX spectrum shown in Fig. 9b, one can observe that the undissolved precipitates have significant amounts of Nb and Ti (quantitative analyzes are not shown here), as well as small amounts of V and Cr. According to the literature [24], it is not expected to find vanadium at elevated temperatures, and the obtained level of vanadium can be assigned to the $Ti_{K\beta}$ and $Cr_{K\alpha}$ peaks, as can be observed in Fig. 9b. Furthermore, it is worth noting the confirmed presence of the Ti peak. The large amount of Cu came from the support copper grid for the carbon film. The indexation of the SAEDP in Fig. 9c, and for all precipitates observed at the end of soaking time, revealed that the undissolved precipitates were Nb–Ti nitride ($Ti_3Nb_7N_{10}$) with face-centered cubic (FCC) crystal structure and lattice parameter of 0.436 nm, independently of the precipitate geometry.

Fig. 10a shows the precipitates extracted after the interpass time from the sample with 10 passes and interpass time of 20 s. In this figure it is possible to note the presence of precipitates of different sizes and shapes (round, square and elongated), and that

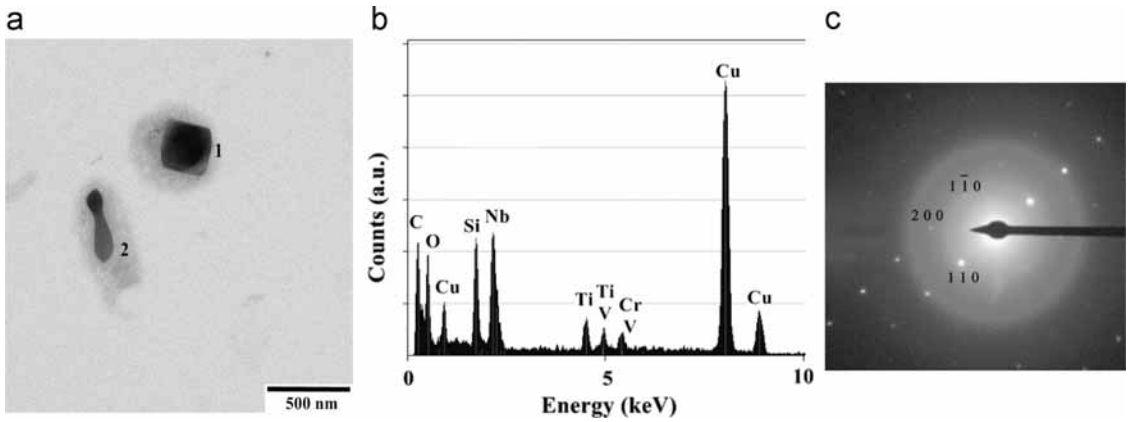

Fig. 9. (a) BF-STEM micrograph for sample at the end of soaking time. (b) EDX analysis of precipitate 1 in (a). (c) SAEDP for such precipitate which is near the [100] zone axis and was indexed as being $Ti_3Nb_7N_{10}$ phase.

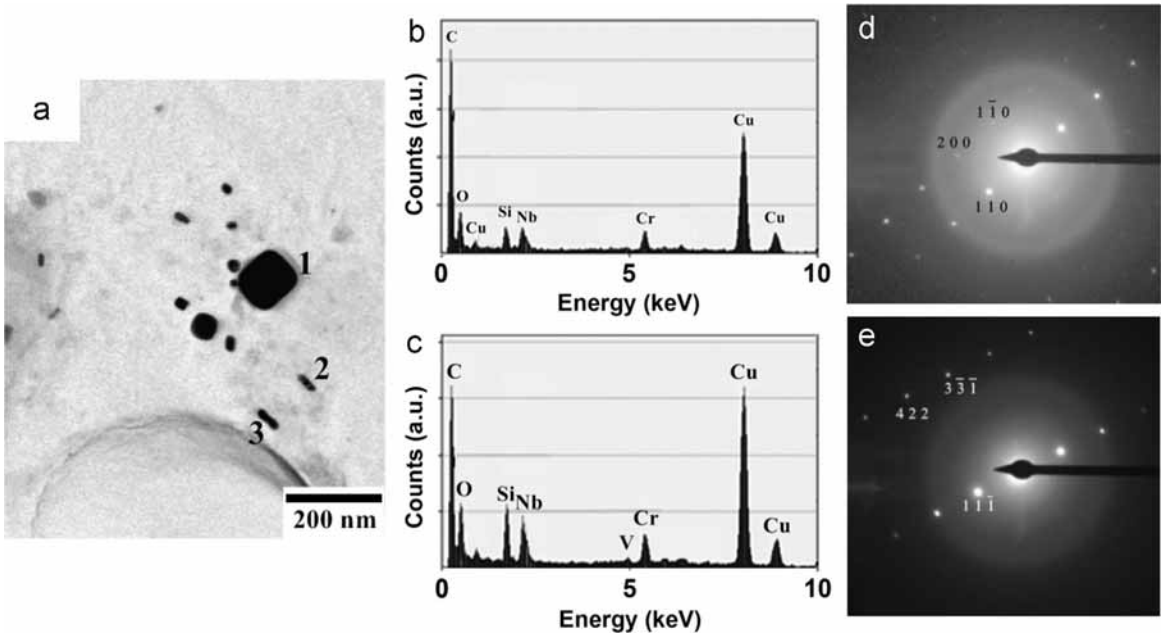

Fig. 10. (a) Bright field STEM image of carbon replica from a sample processed with 10 passes and 20 s of interpass time. EDX and SAEDP analysis: (b) Precipitate 2 presented in (a) and SAEDP for Z-phase near the [001] zone axis, is in the inset. (c) Precipitate 3 in (a) and SAEDP for NbN, near the [213] zone axis, is in the inset.

the smallest precipitates have a diameter of about 40 nm. EDX analyses revealed that only precipitate 1, among the analyzed precipitates in Fig. 10a, had Ti in the composition, suggesting this is an undissolved particle coming from the soaking process. The results for other precipitates showed that they were Cr- and Nb-rich, and the EDX spectra (Fig. 10b and c) confirm the absence of Ti. The indexed SAEDPs of precipitates 2 and 3 are shown in Fig. 10d and e, respectively. Precipitate 2 is a complex CrNb nitride (Z-phase), with a tetragonal crystal structure and lattice parameters of $a=0.304$ and $c=0.739$ nm (the SAEDP is close to the [001] zone axis). Precipitate 3 displayed a higher content of Nb, and the indexation indicates that it is the niobium nitride (NbN), which is fcc with lattice parameter of 0.439 nm (SAEDP close to the [213] zone axis). Only 4.8% of the analyzed particles correspond to NbN, and the majority of the precipitates were formed during processing, including both NbN and Cr- and Nb-rich complex nitrides (Z-phase).

3.4. Interaction between precipitation and recrystallization

In order to analyze the interaction of precipitates with grain boundaries and dislocations, thin foil samples were prepared for the analyzed conditions and some micrographs are illustrated in Fig. 11. Fig. 11(a) shows the precipitates after the soaking time. It is possible to observe that most of the precipitates were solubilized and those which remained insoluble are larger. In this condition, most of the larger particles which were observed have elongated morphology.

Precipitates in the sample with two passes and interpass time of 20 s are shown in Fig. 11b. In this figure is possible to observe that large precipitates were located in grain boundaries or inside them, and, in this condition, larger particles were observed, confirming again that these large (er) particles/precipitates are not effective to pin grain boundaries. Also, dislocation accumulation or dislocation tangles were not observed, confirming that the material was completely recrystallized after only 2 deformations steps at the high temperatures. Fig. 11(c) shows a region of the sample with 10 passes and interpass time of 20 s showing that the fine precipitation is huge, and that they are smaller than with 2 passes. Some dislocation storage can be seen in the right-hand side of the central region of the picture.

The precipitation increases with the decreasing temperature and with the increasing deformation. Particularly, the precipitation was intense after 13 passes, independent of the interpass time. Fig. 11(d) shows an area for the condition of 13 passes and 20 s, where a large fraction of small precipitates (<50 nm) is observed as well as the presence of dislocations within the grains, featuring partial recrystallization of the material. In addition, it is observable how some precipitates are pinning grain boundaries while other particles are heterogeneously dispersed inside the grains. The interaction of the precipitates with grain boundaries, subgrains and dislocations is displayed in the middle left-hand side of Fig. 11e. The last micrograph, Fig. 11f, corresponds to a region of the sample with 13 passes and 5 s and shows a high density of fine precipitates that are distributed on the austenitic matrix, although some of them are pinning grain boundaries.

Table 2 summarizes data of average sizes and recrystallized fractions of grains, average sizes (separated by ranges), particle densities (ρ), volume fraction and type of precipitates for all analyzed conditions, from the previous analyses and figures. Samples with up to 2 passes of deformation were fully recrystallized, and with 81% of high-angle grain boundaries. After the 10th and 13th passes and holding times the material was partially recrystallized as reflected by the fact that less than 60% of high-angle grain boundaries were noticed. These data show that the precipitate-particles densities are low when the material was at high temperatures, and increased significantly below the transition temperature. Furthermore, it is worth noticing that, after 13 passes, the particles' density is slightly greater in 20 s than 5 s, while the volume fraction is 1.6 times bigger. This is probably because in a larger interval between passes both are favored, the precipitation and the particle growth, as demonstrated by ranges of distributions size precipitates.

4. Discussion

Upon thermomechanical treatment, steels are reheated to elevated temperatures, maintained in these temperatures for chemical

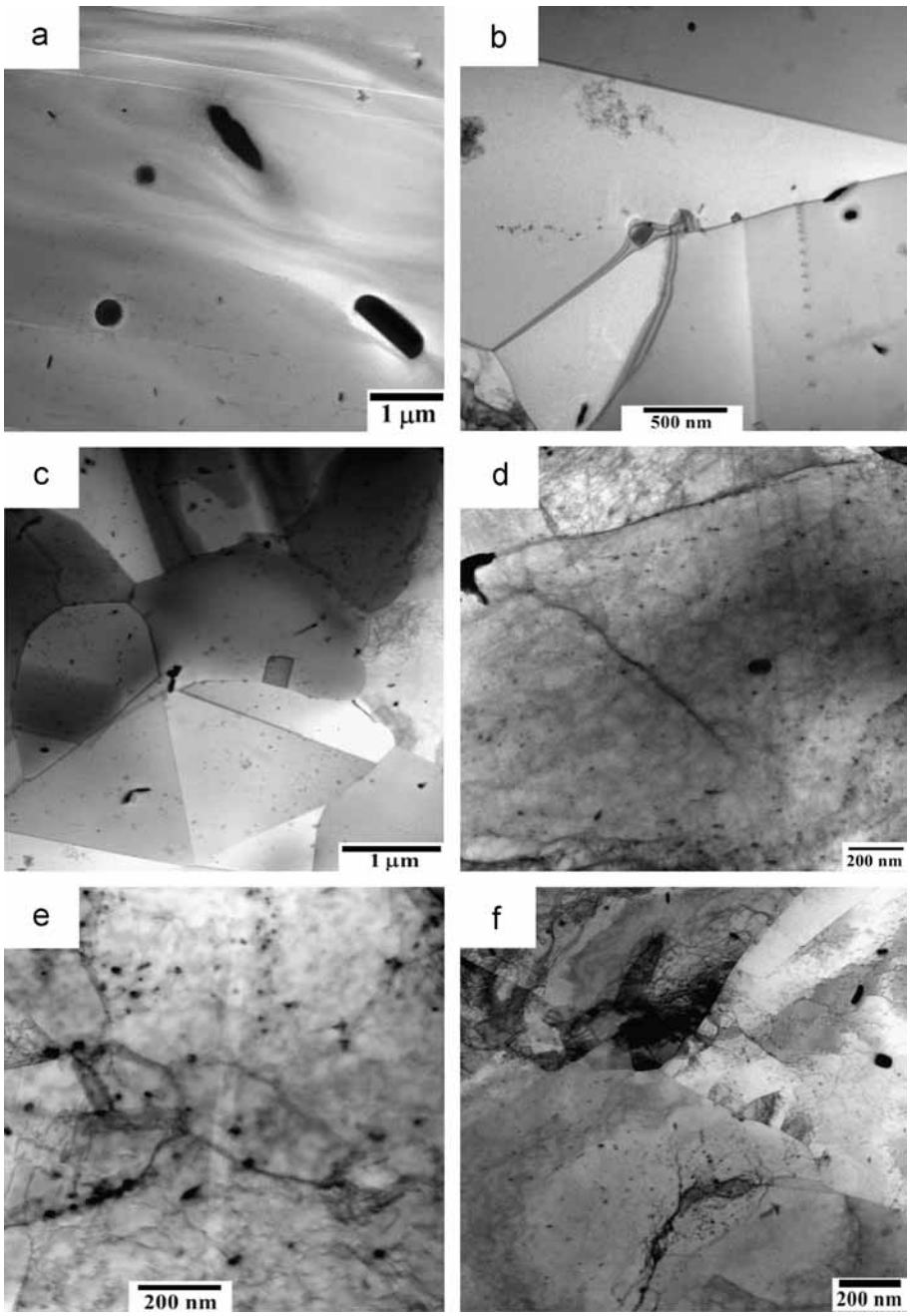

Fig. 11. Thin foils TEM analysis showing precipitates in the following conditions: T_{soak}=1250 °C (5 min) in (a); on cooling with t_{ip}=20 s after the second pass in (b), after 10th pass (c) and after 13th pass in (d) and (e); and after 13th pass with t_{ip}=5 s in (f).

and microstructural homogenization, subjected to deformation schedules on continuous cooling and are finally cooled to room temperature. When ISO 5832-9 was reheated to 1250 °C and maintained in this temperature for 5 min presented a microstructure composed of austenite grain with a mean size of 62 μm and a volume fraction of the 0.97×10^{-3} of undissolved particles. These particles were identified as $Ti_3Nb_7N_{10}$ phase and most of them were larger than 100 nm. In addition, very large particles, not taken into account in our statistics of TEM extracted replicas, were also observed by EBSD and optical microscopy analyses. Thus, in the beginning of the deformation process, most of the Nb was in solid solution and ready to precipitate during the continuous cooling.

During the two first passes, some microstructural change occurred. Fig. 6 shows that immediately after the second deformation, the material is partially recrystallized, suggesting that dynamic recrystallization occurred during deformation. After the interpass time, the material is completely recrystallized, independent of the holding time. One can infer that, at high temperatures, the material is completely recrystallized at the end of the interpass time and there is no strain accumulation from pass to pass. Along with the softening mechanism, there is some increase in the amount of particles. The volume fraction of particles and the particle density are close to twice as great. Since the material is completely recrystallized, one can speculate that at higher temperatures the present precipitates cannot inhibit the recrystallization.

During the deformation schedule the particle density increases. After 2 passes, the density is twice the original one, but the increase is larger when the temperature decreases below to the transition temperature. After the 13th pass the particle density increased around 44 times when compared with that presented after the soaking time,

Table 2
Data of average grain sizes, average precipitate sizes (separated by ranges of size), recrystallized fractions, particle densities (ρ), volume fraction and type of precipitates for all the analyzed conditions.

		Grains		Precipitates				
		d (μm)	Recryst. fraction	d (nm)	Distributions (%)	ρ (part/μm^2)	Vol. fraction	Type
As received		14.4 (4.7)	–	–		–	–	–
1250 °C/5 min		61.8 (34.4)	–	133.03 (95.84)	< 20 nm–0.88 20–50 nm–13.72 50–100 nm–29.65 > 100 nm–55.75	0.32	0.97×10^{-3}	TiNbN
20 s	**2 passes**	32.6 (20.9)	0.81	102.72 (65.71)	< 20 nm–2.38 20–50 nm–21.90 50–100 nm–34.29 > 100 nm–41.43	0.56	1.80×10^{-3}	TiNbN Z-phase
	10 passes	11.8 (5.9)	0.43	55.03 (34.93)	< 20 nm–6.07 20–50 nm–53.44 50–100 nm–29.55 > 00 nm–10.93	3.49	2.59×10^{-3}	TiNbN Z-phase NbN
	13 passes	9.5 (4.4)	0.57	38.64 (24.12)	< 20 nm–13.82 20–50 nm–66.55 50–100 nm–16.36 > 100 nm–3.27	14.18	4.56×10^{-3}	TiNbN Z-phase NbN
5 s	**2 passes**	25.8 (8.8)	0.81	95.89 (64.17)	< 20 nm–11.49 20–50 nm–14.47 50–100 nm–32.34 > 100 nm–41.70	0.77	1.87×10^{-3}	TiNbN Z-phase
	13 passes	5.1 (2.1)	0.57	32.19 (25.28)	< 20 nm–36.82 20–50 nm–45.61 50–100 nm–15.20 > 100 nm–2.26	13.83	2.78×10^{-3}	TiNbN Z-phase NbN

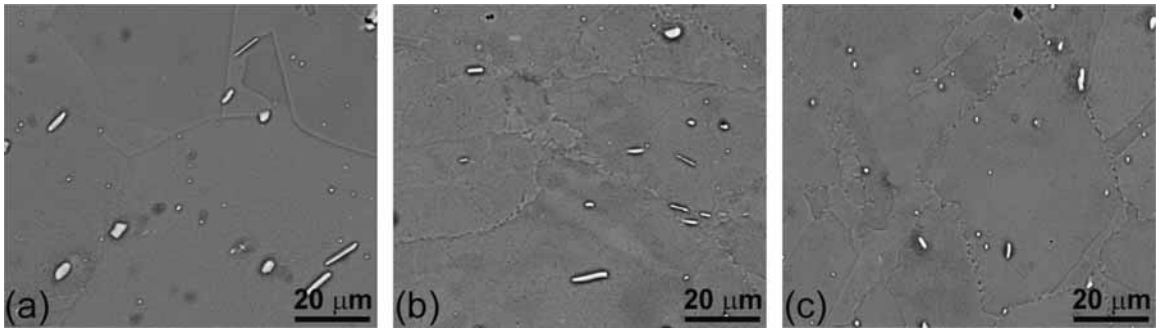

Fig. 12. SEM micrographs showing the evolution of large particles after (a) the soaking time, (b) the second pass and (c) the sixth pass.

and the amount of precipitates smaller than 50 nm are almost the same for both interpass times. Data displayed in Table 2 indicated that in all conditions the TiNbN phase was present. Taking into account that this phase was already there after the soaking time as larger and undissolved particles and the relative volume fraction of particles with size greater than 100 nm decreased during processing, one can infer that precipitation of this phase did not occur during cooling. Thus, the increases of precipitation can be attributed to NbN and Z-phase, mainly Z-phase.

It is well established that small particles interact with dislocations inhibiting their movement. Fig. 11d and e shows small particles interacting with dislocation and grain boundaries during the interpass time after 10 and 13 passes. This interaction inhibits the recovery and the onset of recrystallization during interpass times and, so, the dislocation density does not decrease during this period. Consequently, as displayed in Fig. 2, there was strain accumulation for the next pass and the slope of the MFS vs. $1/T$ diagram, below the transition temperature, increased. Thus, the precipitates retard recrystallization, causing strain accumulation that thickens grain boundary areas, which are the main nucleation sites for new grains, providing preferential areas for recrystallization on subsequent passes.

The grain size evolution during deformation on continuous cooling conditions is noticeable. The grain size is reduced by half after the second pass. After 13 passes, the grains size is reduced by 6.5 times, for tests conducted with interpass time of 20 s, and by 12.1 times for interpass time of 5 s. It is worth noting that the reduction of four times in the interpass time led to a grain refinement almost twice higher. This is significant, because this steel is totally austenitic and no phase transformation takes place as it occurs in ferritic materials, where this transformation allows further grain refinement. The recrystallized volume fraction also has different behaviors at the beginning and after several deformations. After the second pass, the material is completely recrystallized, but the recrystallized volume decreases as the deformation proceeds, when compared with the initial ones.

Particles of Z-phase and NbN, precipitated during the processing, showed rapid growth at elevated temperatures and thus they are not efficient for pinning grains at temperatures higher than 1110 °C. The change in the slope of the curves of MFS vs. $1/T$

diagram was associated with a transition from a complete recrystallization region to another region of partial recrystallization, analogous to the non recrystallization temperature (T_{nr}) observed in microalloyed steels.

However, by comparing mechanical behaviors, one will observe two interesting different comportments between the ISO 5832-9 and the microalloyed steels. Firstly, it was not noticed distinctly elongated grains in the microstructures of ISO 5832-9, as they are in the microalloyed ones. In the steel ISO 5832-9, at lower temperatures, the grains are slightly elongated (as seen in Fig. 3e and f and better visualized in Fig. 5). This behavior may be resulting from a fast dynamic recrystallization already present in the early stages and further passes, finally providing an excellent grain refinement.

Secondly, there are only two regions of stresses in microalloyed steels and both will grow monotonically. Inside the first region (highest temperatures) the stresses will grow until reaching the T_{nr}, where fine precipitation starts and where a characteristic change of the stress growth-slope will occur. In the case of the ISO 5832-9, at highest temperatures, there is the presence of a region with a negative slope (region I, Fig. 2) before a monotonic growth to a transition temperature (region II, Fig. 2).

Under the above context, one can say that there was first strain hardening followed by a plentiful softening due to dynamic recrystallization, as observed in Fig. 6. When describing Fig. 6c, we have hypothesized a particle reinforcement of the matrix, before a total breakage and redistribution of non-dissolved particles, as the possible mechanism for the first two passes. In order to confirm this hypothesis, we have performed SEM analysis in the soaked condition and after second and sixth passes to study the evolution of the larger particles. In addition, microhardness measurements were performed on larger particles+matrix and on smaller-broken particles+matrix, to have one idea about the stress fields around these particles, which will possibly be concluding about strain hardening inside region I, and also the consequent effect on the recrystallization. Fig. 12 shows SEM micrographs of the above conditions where it is possible to observe clearly that, after soaking, the number of particles is smaller and that the particle sizes are larger than in the two other conditions (second and sixth passes). In addition, the particle sizes are more homogeneous and better distributed after the sixth pass when compared with the soaked and second-pass conditions.

Microhardness measurements gave the value of 346 ± 22 HV for larger particles+matrix and 271 ± 11 HV for smaller-broken particles+matrix. In other words, in the first pass, with mostly the presence of larger particles, the stress field (and, consequently, the work-hardening) is more intense than in the second and further passes, where the particles are already broken and redistributed. This extra work-hardening, produced by the largest particles, will lead to a higher stresses as the ones observed in the first two passes for 5 and 20 s of interpass time. Of course, in these conditions, the material will reach the critical deformation for dynamic recrystallization earlier and leading to a more intense recrystallization. After breaking and redistributing the particles in the second pass, the stress fields will become smaller than in the first, decreasing the work-hardening, however, still reaching earlier the critical deformation and thus dynamic recrystallization will continue being more effective than in the further passes. This, in fact, is indicating that there was the formation of a "new material" after the second pass, with a very well distribution of the smaller-broken particles, thus homogenizing the stress and the deformation in the subsequent passes, leading this fresh material to a similar behavior as for the microalloyed one.

5. Conclusions

A high niobium- and nitrogen-bearing austenitic stainless steel (ISO 5832-9) was deformed by hot torsion tests simulating rolling processing. Under industrial testing conditions, the influence of interpass time on grain refinement was planned. Specifically, the interaction between recrystallization and strain induced precipitation for two distinct interpass times was studied. The main conclusions which may be drawn are as follows:

1. The differences in the obtained stress levels can be a direct consequence of grain refinement together with precipitation that makes the deformation difficult, since the mechanisms that act on each pass are the same.
2. Interpass time exerts influence on grain and precipitate sizes, acting directly in the process of recovery, recrystallization and precipitation. The shorter interpass time led to smaller sizes of grains and precipitates. Precipitates with sizes smaller than 50 nm were efficient to pin grain boundaries and dislocations. The greater the fraction of small particles (< 50 nm) the greater the microstructural refinement.
3. The steel ISO 5832-9 recrystallizes dynamically. Dynamic recrystallization is already present even at high temperatures (~ 1190 °C) after two deformations of 0.3.
4. After homogenization, only precipitates of TiNbN were found. During hot deformation, precipitates of Z-phase and NbN were formed, being the last in a smaller amount (only 4.8%). Precipitates with different morphologies were analyzed, and it was found that there is no correlation between the morphology and chemical composition.

Acknowledgments

The authors are grateful to CNPq, (Conselho Nacional de Desenvolvimento Científico e Tecnológico) under the grant CNPq# 506440/2013-3, FAPESP (Fundação de Amparo à Pesquisa do Estado de São Paulo) and CAPES (Coordenação de Aperfeiçoamento de Pessoal de Nível Superior), under the grant CAPES#179/09 for the financial support received in involved projects and Villares Metals, São Paulo-Brazil, that supplied the steel. As well authors are grateful to CNPq (Brazil) and Ministerio de Educacion (Spain) for funding a bilateral cooperation, under the cooperation project CAPES#179/09.

References

[1] K.H. Lo, C.H. Shek, J.K.L. Lai, Mater. Sci. Eng. R 65 (2009) 39–104.
[2] J. Menzel, W. Kirschner, G. Stein, ISIJ Int. 36 (1996) 893–900.
[3] J.W. Simmons, Mater. Sci. Eng. A 207 (1996) 159–169.
[4] Y.J. Oh, J.H. Hong, J. Nucl. Mater. 278 (2000) 242–250.
[5] H. Hanninen, J. Romu, R. Ilola, J. Tervo, A. Laitinen, J. Mater. Process. Technol. 117 (2001) 424–430.
[6] R.C. Souza, E.S. Silva, A.M. Jorge Jr, J.M. Cabrera, O. Balancin, Mater. Sci. Eng. A 582 (2013) 96–107.
[7] C.L. Miao, C.J. Shang, G.D. Zhang, S.V. Subramanian, Mater. Sci. Eng. A 527 (2010) 4985–4992.
[8] S. Vervynckt, K. Verbeken, B. Lopez, J.J. Jonas, Int. Mater. Rev. 57 (2012) 187–207.
[9] T. Gladman, Proc. R. Soc. Lond. 294 (1966) 298–309.
[10] P. Manohar, M. Ferry, T. Chandra, ISIJ Int. 38 (9) (1998) 913–924.
[11] W.P. Sun, M. Militzer, D.Q. Bai, J.J. Jonas, Acta Metall. Mater. 41 (1993) 3595–3604.
[12] P. Hellman, M. Hillert, Scand. J. Metall. 4 (1975) 211–219.
[13] R. Abad, A.I. Fernández, B. López, J.M. Rodriguez-Ibabe, ISIJ Int. 41 (2001) 1373–1382.
[14] M. Gómez, S.F. Medina, P. Valles, ISIJ Int. 45 (2005) 1711–1720.

[15] E.J. Giordani, A.M. Jorge Jr, O. Balancin, Mater. Sci. Forum 500–501 (2005) 179–186.
[16] C. Örnhagen, J.-O. Nilsson, H. Vannevik, J. Biomed. Mater. Res. 31 (1996) 97–103.
[17] A.J. Deardo, Ironmak Steelmak 28 (2001) 138–144.
[18] H. Chilukuru, K. Durst, S. Wadekar, M. Schwienheer, A. Scholz, C. Berger, K.H. Mayer, W. Blum, Mater. Sci. Eng. A 510-511 (2009) 81–87.
[19] R.J. Seher, H.M. James, G.N. Maniar, Symposium: American Society for Testing and Materials, 1971, pp. 119–137.
[20] ⟨http://cimewww.epfl.ch/people/stadelmann/jemsWebSite/jems.html⟩.
[21] F. Boratto, R. Barbosa, S. Yue, J.J. Jonas, in: International Conference on Physical Metallurgy of Thermomechanical Processing of Steels and Other Metals (Thermec-88), ISIJ, Tokyo, Japan,1988, pp. 383–390.
[22] T. Sakai, A. Belyakov, R. Kaibyshev, H. Miura, J.J. Jonas, Prog. Mater. Sci. 60 (2014) 130–207.
[23] T. Sakai, J. Mater. Process. Technol. 53 (1995) 349–361.
[24] E.V. Morales, J. Gallego, H. –J. Kestenbach, Philos. Mag. Lett. 83 (2003) 79–87.